Materials Advances

ROYAL SOCIETY OF CHEMISTRY

PAPER

View Article Online
View Journal

Cite this: DOI: 10.1039/d5ma01270h

DFT insights into nano-Au/carbon nitride: potent CO oxidation facilitated by weak metal–support interaction

Milad Behroozi,[ab] Esmail Doustkhah *[ab] and M. Hussein N. Assadi *[ac]

Received 2nd November 2025,
Accepted 22nd December 2025

DOI: 10.1039/d5ma01270h

rsc.li/materials-advances

The catalytic performance of gold nanoparticles is critically dependent on the nature of the heterogeneous support used. Spin-polarised density functional theory (DFT) calculations with dispersion corrections (DFT-D3) were employed to investigate 1-, 2-, 4-, and 8-layer Au nanosheets supported on cubic C_3N_2 ($Au_x@C_3N_2$). Crucially, the near-Fermi-level Au 5d band, which is vital for catalytic turnover, remains essentially unchanged across all thicknesses, confirming that the metal's electronic population is largely insensitive to the C_3N_2 substrate. Charge density and electron localisation function analyses confirm that the interface is governed by weak van der Waals forces, evidenced by Au-support separations of approximately 3 Å and negligible mid-bond charge, ruling out covalent or metallic bonding. This weak interaction prevents electron deficiency in the Au atoms, enabling miniaturisation into the sub-nanometre regime. Among the configurations examined, the four-layer nanosheet offers the highest near-E_{Fermi} 5d occupation, preserving the high intrinsic activity required for potent CO oxidation.

1. Introduction

Au, one of the most common noble metals, is widely used in heterogeneous catalysis.[1–3] However, it requires delicate nanoengineering (*e.g.*, thickness and shape) and a careful choice of support to minimise the loading amount.[4,5] For such nanoarchitectures, the thickness, shape, and facet orientation of Au, as well as the support material, play critical roles in determining catalytic activity.[6,7] It is well accepted that the support nature can drastically influence the catalytic activity of the deposited metal through the electronic interactions in the interface of the metal and the support.[8] The interface interaction can consequently affect factors like surface energy, electron density, and chelation affinity of the outermost layer of the deposited metal.[9] Despite the current trend of minimising the size of the loaded metal nanoparticles toward a single atom, in some cases, electrons from the metal atoms can transfer to the support, through hybridisation, leading to electron deficiency, and consequently, a decrease in the catalytic activity. The electron deficiency in the metal can be more detrimental in smaller (sub-nanometre) metallic nanoparticles.[10]

According to previous investigations, depositing Pd on silicate layers can significantly reduce the metallicity of Pd atoms at the interface between the thin Pd nanosheets and the silicate support.[10] Therefore, to achieve a proper metallicity in the Pd nanosheets, at least six atomic Pd layers are required to produce H_2 from formic acid efficiently.[11,12] This electron deficiency arising from the metal–support interaction can particularly prevent metals from exhibiting competitive catalytic activity when synthesised in single-atom form. On the orbital scale, this deficiency arises from the hybridisation of the d orbitals of the noble metal with the p or s orbitals of the support elements, resulting in ionic electron transfer or covalent electron sharing,[13] which can reduce the catalytically labile d electrons. For example, high covalent bonding between Pd and its oxide support surface negatively impacts Pd's catalytic activity.[10] In some cases, however, a robust metal–support interaction can positively impact the cyclability of the catalyst, increasing its lifetime.[14] It is therefore imperative to investigate thoroughly how the metal size depends on the support's nature, composition, and crystal structure.

CO oxidation on Au is a representative reaction that highlights the catalytic potential of Au species. The synthesis of gold nanoclusters (*e.g.*, Au_{10}, Au_{20}, Au_{38}) is now well established through several methods.[15,16] However, further progress towards industrial applications requires careful optimisation

[a] *Chemistry Department, Faculty of Engineering and Natural Sciences, Istinye University, Sariyer, Istanbul 34396, Türkiye.*
E-mail: esmail.doustkhah@istinye.edu.tr, h.assadi.2008@ieee.org
[b] *Clean Energy Research Center (TEAM), Istinye University, Sariyer, Istanbul 34396, Türkiye*
[c] *RIKEN Center for Emergent Matter Science (CEMS), 2–1 Hirosawa, Wako, 351–0198 Saitama, Japan*

of the metal–support interface.[17–19] Accordingly, we investigated the layer-resolved density of states (DOS) of single-, two-, four-, and eight-layer gold nanosheets supported on carbon nitride to examine the electronic modifications induced by the support and their influence on catalytic activity. The DOS results reveal that, unlike other noble metals such as Pt, the metallic character of Au is considerably less affected by the carbon nitride support, even in the initial layers at the metal–support interface.

2. Computational settings

We conducted spin-polarised density functional theory (DFT) calculations employing the Vienna *ab initio* simulation package (VASP) with projector-augmented wave potentials.[20–22] To incorporate dispersion effects, we utilised the DFT-D3 level of theory following the Grimme scheme.[23,24] The generalised gradient approximation was employed to approximate the exchange–correlation functional.[25] The energy cutoff was set to be 550 eV, and the Brillouin zone was sampled using a $3 \times 3 \times 1$ Monkhorst–Pack mesh. The pseudopotentials contained the following valence electrons: $2s^2 2p^2$ for C; $2s^2 2p^3$ for N; $2s^2 2p^4$ for O; $1s^1$ for H; and $5d^{10} 6s^1$ for Au. The residual minimisation method, direct inversion in the iterative subspace (RMM-DIIS) algorithm, was used to achieve fast, consistent electronic convergence, with projection operators evaluated in real space. The adequacy of these settings for carbon-metal systems was established in our prior works.[26,27]

Structural optimisation was performed meticulously to ensure force components smaller than 0.01 eV $Å^{-1}$ and an energy threshold of 10^{-7} eV. Both interface components (Au and C_3N_2) were first allowed to relax fully, including the cell parameters. However, for the interface structure, the cell volume was fixed to maintain the vacuum slab during the geometry optimisation. The partial occupancies f_{nk} were determined using the Methfessel–Paxton scheme during geometry optimisation, as this scheme accommodates partial occupancies, which might be the case for metals (Au in our case). Here, the smearing width was 0.05 eV. Density of states (DOS) was calculated using the tetrahedron method with Blöchl corrections, which is believed to produce more accurate DOS. To investigate the bonding characteristics between Au nanosheets and the adsorbed species, crystal orbital Hamiltonian population (COHP) analyses were performed using the LOBSTER v5.1.1 package.[28–30] Bader charge analysis was carried out using the near-grid algorithm developed by Henkelman *et al.*[31] applied to charge-density files generated by VASP, with the electron density evaluated on a uniform grid of 7 points $Å^{-1}$.

3. Results and discussion

The first step in simulating the interface between gold nanosheets and carbon nitride is selecting a computationally feasible $C_\delta N_\epsilon$ structure with an acceptable lattice mismatch to Au. Such a choice is necessary to produce an experimentally plausible and numerically tractable configuration. For this purpose, we selected the cubic C_3N_2 structure reported in the literature (Materials Project ID = mp-1188347).[32] This carbon nitride structure is cubic with space group $P\bar{4}3m$ and a cell parameter of 5.085 Å, comparable to that of face-centred cubic Au, which is 4.0873 Å. For building the simulation box, the C_3N_2 structure was cleaved along a lattice direction and extended to form a $2u \times 1v$ facet that was two-unit-cell deep. On one side of the C_3N_2 facet, 1, 2, 4, 8 layers of cubic Au, each containing 8 Au atoms, were added to simulate the $Au_x@C_3N_2$ interface. The C atoms with dangling bonds on the opposite facet were neutralised with OH groups. Finally, an ample vacuum slab was added to impose the isolation of the Au surface from C_3N_2's periodic image and aid convergence.

Ultimately, the unit cell compositions were $Au_8C_{48}N_{32}(OH)_4$, $Au_{16}C_{48}N_{32}(OH)_4$, $Au_{32}C_{48}N_{32}(OH)_4$, and $Au_{64}C_{48}N_{32}(OH)_4$, respectively. For the 8-layer configuration, the unit cell, upon relaxation, was orthogonal, with a = 10.171 Å, b = 5.085 Å, and c = 70.585 Å. However, for the remaining configurations, the relaxed unit cells were slightly slanted; the lattice parameters are reported in Table S1, while full geometries are provided in the supplementary information. Structurally, in pristine Au, atoms within any given layer share a common z coordinate. In $Au_x@C_3N_2$, bonding to the chemically heterogeneous C/N support lifts this geometric symmetry, and Au atoms that initially possessed identical z values relax to slightly different heights. To retain a physically meaningful and comparable layer definition across thicknesses, Au atoms were reassigned to layers whenever their mutual z disparity was ≤ 1 Å. This criterion was adopted after verifying that atoms grouped within this proximity exhibit nearly indistinguishable DOS profiles, thereby streamlining the analysis without sacrificing accuracy. The resulting layer order in each Figure proceeds from the vacuum-exposed surface down to the interface-proximal layer. This consistent protocol enables direct, thickness-dependent comparison of the Au 5d electronic structure at and away from the interface.

According to Fig. 1a and b, the relaxed Au monolayer stands at a vertical distance of 3.25 Å above the C_3N_2 substrate. The spacing is characteristic of a comparatively weak Au-support coupling, suggesting physisorption-type interactions. The DOS of the Au 5d states (Fig. 1c) has minimal overlap with those of the substrate C and N atoms (Fig. 1d and e), reflecting the absence of strong hybridisation between the Au layer and the substrate. Consequently, the Au monolayer interacts weakly with the C_3N_2 surface, leading to minimal perturbation of the support's electronic structure. The relaxed two-layer Au film, as referred to in Fig. 2, is structurally a nanosheet approximately 2.85 Å thick, positioned 2.99 Å from the C_3N_2 support. This separation distance indicates intermediate Au-substrate coupling, stronger than that at the monolayer, though weaker than in other configurations studied here. The layer-resolved Au 5d DOS (Fig. 2c and d) shows that the electronic structure remains largely unperturbed, with only slight differences between the vacuum-exposed and interfacial layers. This observation is reinforced by the partial DOS of the interfacial C and N atoms

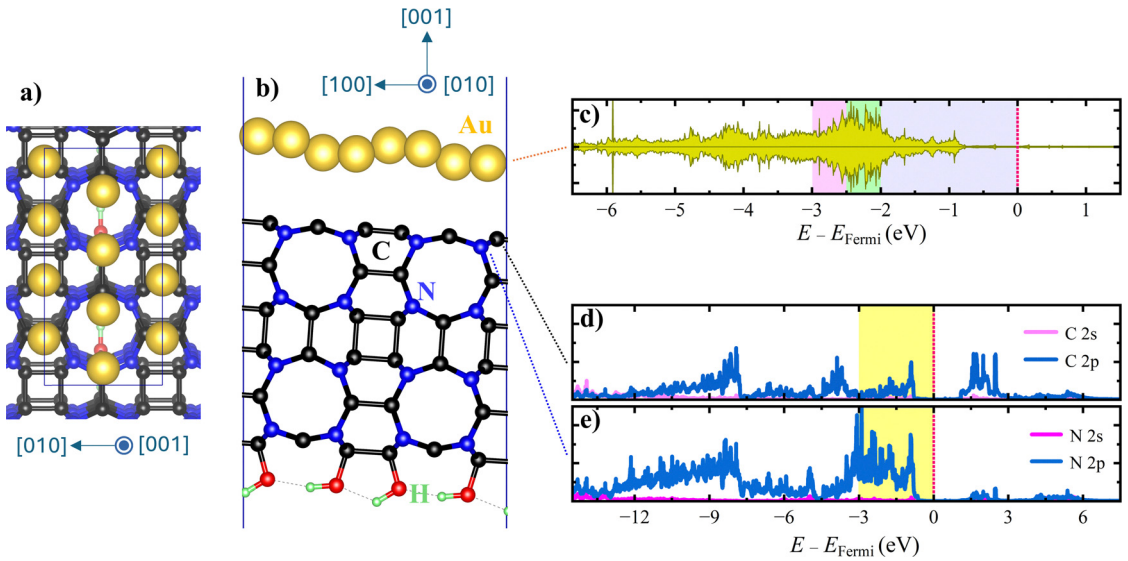

Fig. 1 (a) and (b) Top and side views of the optimised structure of the single-layer Au nanosheet supported on C_3N_2. (c) The partial Au 5d density of states; the DOS outside the presented energy range is negligible. (d) and (e) The partial 2s and 2p DOS of the interface C and N, respectively.

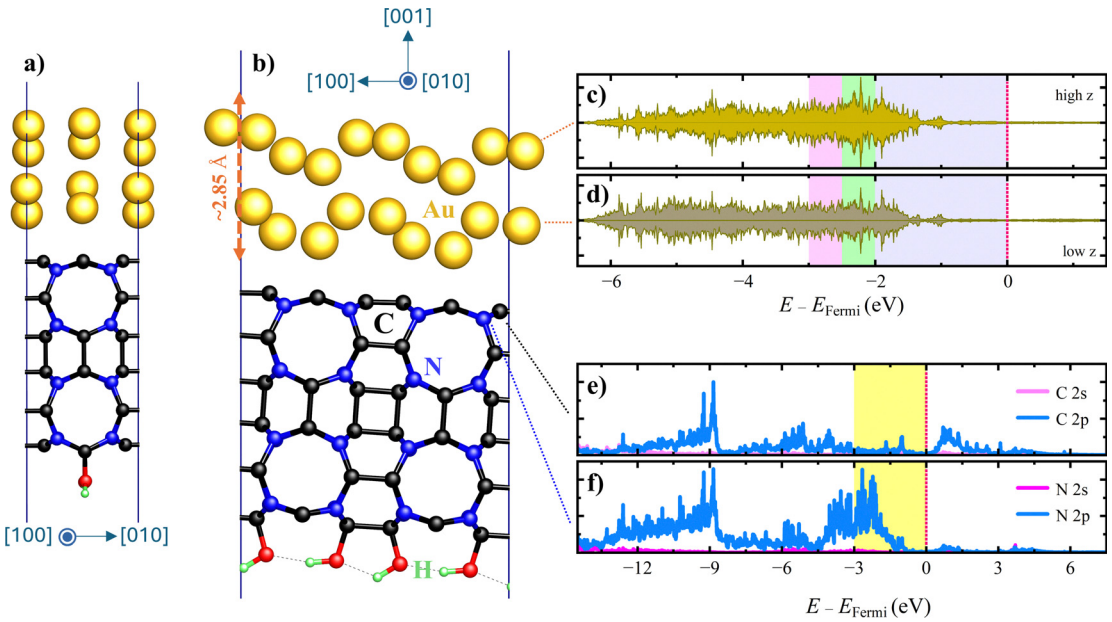

Fig. 2 (a) and (b) Different side views of the optimised structure of the Au nanosheet supported on C_3N_2. (c) and (d) The partial Au 5d density of states resolved by layers. Au 5d DOS outside the presented energy range is negligible. (e) and (f) The partial 2s and 2p DOS of the interface C and N, respectively. *z* denotes the Au atoms' fractional coordinates along the long edge.

(Fig. 2e and f), which verifies minimal charge redistribution at the interface, consistent with the expected gradual buildup of Au_x-C_3N_2 electronic interactions with increasing film thickness.

According to the geometry optimisation results (Fig. 3a and b), the four-layer Au film produced a total thickness of 10.02 Å and an interfacial separation of 3.47 Å from the C_3N_2 substrate. That increased separation means weaker interfacial coupling than in thinner structures. The layer-resolved DOS (Fig. 3c–f) shows a progressive return to bulk-like electronic features in the inner Au layers, while the projected DOS of interfacial C and N atoms (Fig. 3g and h) reveals limited hybridisation. According to Fig. 4a and b, the 8-layer Au film relaxed into a nanosheet with an approximate thickness of 27.42 Å. The interfacial distance between the Au nanosheet and the C_3N_2 support was predicted to be 2.91 Å, which is notably larger than the distances reported for Pd–silicate (1.910 Å)[10] and Eu–titania (1.774 Å) interfaces, suggesting a possibly weaker chemical interaction between gold and its support compared with other

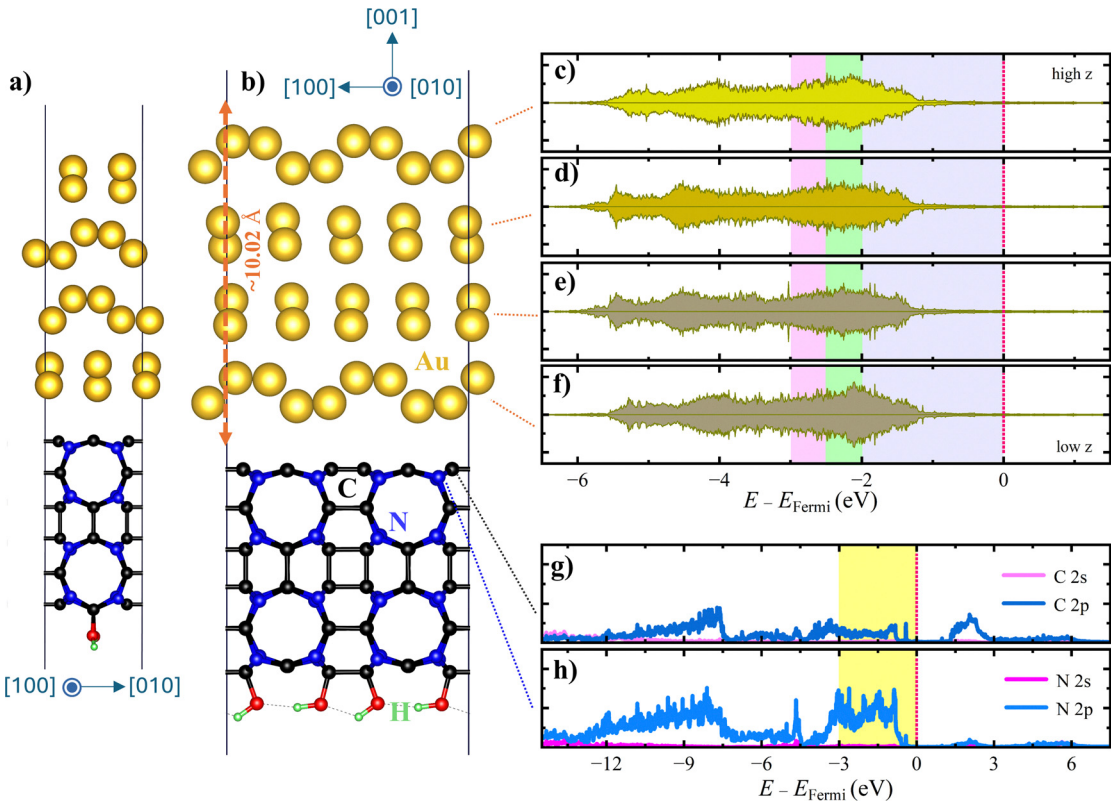

Fig. 3 (a) and (b) Different side views of the optimised four-layer $Au_x@C_3N_2$ interface. (c) through (f) The partial Au 5d density of states resolved by layers. (g) and (h) The partial 2s and 2p DOS of the interface C and N, respectively. *z* denotes the Au atoms' fractional coordinates along the long edge [001].

transition metals. However, this distance is comparable to that between Au and graphite (3.310 Å), which is purely a van der Waals system.[33] Therefore, the Au_x/C_3N_2 interface is likely dominated by van der Waals interactions.

Having obtained the layer-resolved 5d PDOS, we can now make predictions about Au's catalytic behaviour in $Au_x@C_3N_2$. The d-band theory, a fundamental concept in catalysis science, governs the catalytic performance of transition metals.[34] According to this theory, the catalytic activity of a transition and noble metal is intricately related to the availability of d orbitals on their surfaces. These orbitals interact with the molecular orbitals of reactant species, forming new hybrid orbitals that facilitate bond formation and lower the activation energy of catalytic reactions. Detailed descriptions regarding these mechanisms for CO oxidation on the Au surface are provided in the supplementary information (Fig. S1–S5). Ultimately, two key parameters underpin this theory: the occupancy of the d orbitals and the position of the d-band within the valence band.[35] Both characteristics are reflected in the layer-resolved PDOS of the Au 5d states calculated here.

The d-band theory, pioneered by Hammer and Nørskov in the mid-1990s,[36,37] is a fundamental framework in heterogeneous catalysis that relates the electronic structure of transition metals to their catalytic activity.[38] The theory posits that the position of a metal's d-band relative to the Fermi level, particularly the d-band centre (ε_d), serves as a key descriptor for predicting the strength of adsorbate (reactive intermediate) binding to the catalyst surface.[39,40] Specifically, when adsorbate atoms interact with a metal surface, the metal's d-orbitals hybridise with the adsorbate's orbitals, forming bonding and antibonding molecular orbitals. A higher d-band centre typically results in stronger adsorption because it reduces the filling of the repulsive antibonding states. Conversely, a lower d-band centre weakens the adsorbate-metal interaction by increasing the occupancy of antibonding orbitals, thereby destabilising the adsorbate and facilitating its desorption and transformation into products.

Consequently, the d-band centre model elegantly captures this principle by providing a quantitative electronic descriptor that correlates adsorption energies with catalytic performance across different metals and alloys.[41] Beyond the conventional d-band centre, more elaborate and modified descriptors have been proposed, such as the upper d-band edge[42] and alloy-corrected d-band metrics[43] to account for the shape of the d-band density of states, improving predictions particularly for alloy catalysts. This electronic structure perspective has proven invaluable for rational catalyst design, enabling researchers to tune catalytic activity through compositional modifications, strain engineering, or support interactions that systematically shift the d-band position.[34,44]

In the substrate-supported catalysts examined here, two factors can shift the Au 5d states deeper into the valence band, thereby diminishing catalytic activity. The first is hybridisation with the substrate: when the catalyst–substrate interaction is

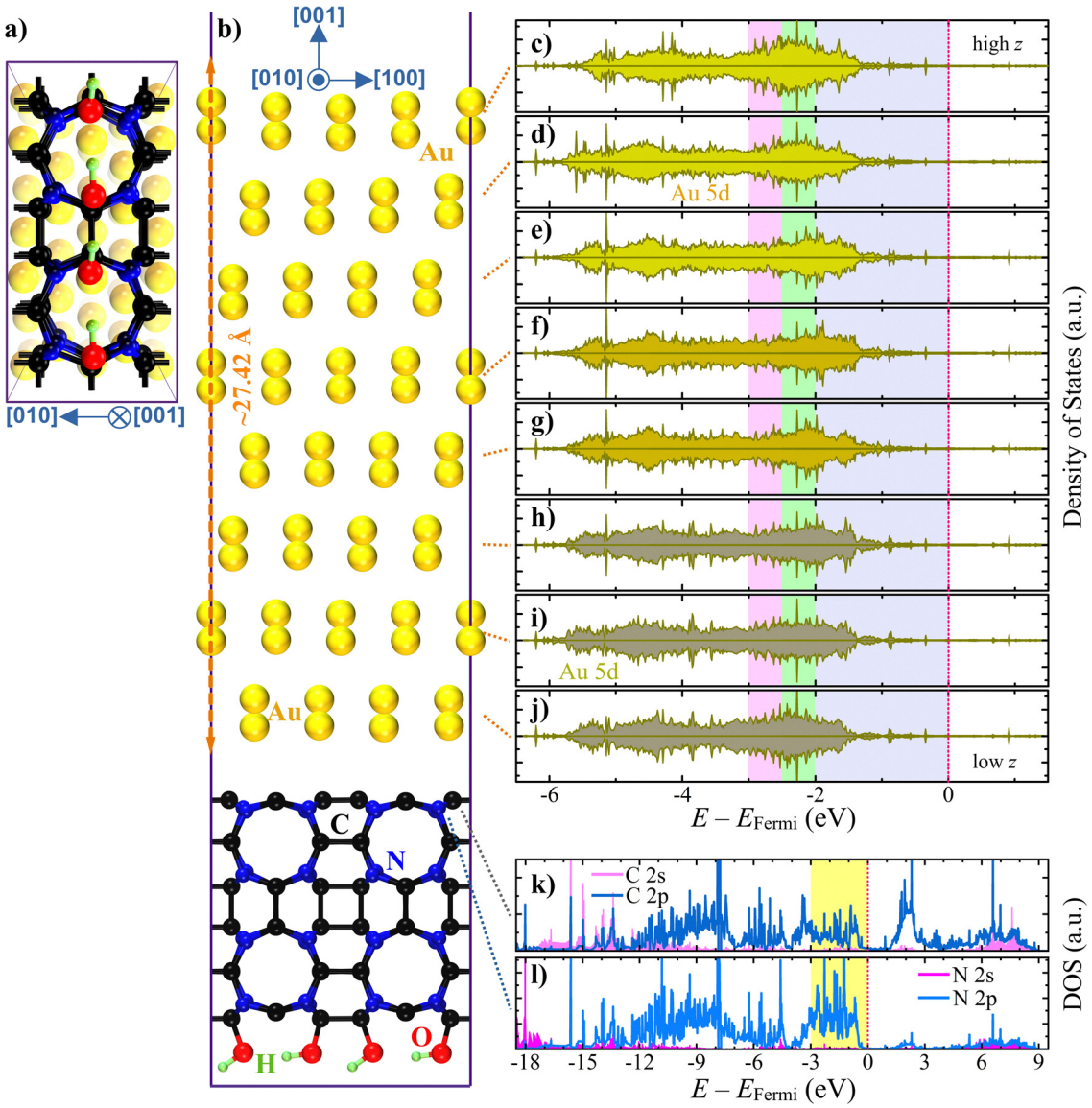

Fig. 4 (a) and (b) Top and side view of the optimised structure of the Au nanosheet supported on C_3N_2. (c) through (j) The partial Au 5d density of states resolved by layers. Au 5d DOS outside the presented energy range is negligible. (k) and (l) The partial 2s and 2p DOS pertaining to the interface C and N, respectively. *z* denotes the Au atoms' fractional coordinates along the long edge.

covalent, the shared electrons occupy lower-energy states and move further from the Fermi level. The second is the confinement effect associated with nanoscale structuring, which can potentially push a fraction of the 5d electrons deeper into the valence band by removing degeneracy. As a result, the fraction of the 5d states just below the Fermi level becomes a more reasonable measure when comparing the lability of the Au 5d electrons in different configurations. Although the bandwidth of these labile electrons is not known *a priori*, it is generally estimated to lie between 2 and 3 eV below E_{Fermi}. However, there is no clear consensus in the literature on which energy interval contains the most labile electrons for general redox reactions; values of −1.64 eV,[45] −2 eV,[46] and −3 eV[47] have been used as cutoffs to assess electron lability. To account for this variability, we integrated the 5d PDOS over three ranges, *i.e.*, [−3 eV, 0], [−2.5 eV, 0], and [−2 eV, 0]. The results are reported in Table 1.

According to Table 1, the electronic 5d population near the Fermi level, across configurations and layers within each configuration, does not show significant variation. For instance, the standard deviation of the 5d population at [−3, 0] across layers in the 4- and 8-layer configurations is 0.2 *e*/Au, indicating a relatively uniform distribution across layers. This uniformity in the distribution of the density of states starkly contrasts with that of other transition-metal nanosheets, such as Ni or Pd, when supported on oxide substrates. In those cases, the d states can increase by more than ∼1.5 electrons per atom within just a few layers from the interface with the supporting material.[10,48]

A more detailed examination of the 8-layer configuration reveals that the variability in the 5d electronic population

Table 1 Layer-resolved electronic population for the occupied Au 5d states for the studied nanosheets. Layer indices and their positions relative to the Au_x@C_3N_2 interface are specified in the corresponding Figures. The reported populations are per Au atom. Column "All" provides the total 5d occupation integrated across the valence band. The remaining three columns provide the 5d occupation integrated within the [−3, 0], [−2.5, 0], and [−2, 0] eV energy ranges, respectively. The Fermi level (E_{Fermi}) is set at 0 for all configurations. z is the fractional Au position along the supercell's long axis

Configuration	Layer	All	[−3,0]	[−2.5,0]	[−2,0]
Single-layered	1	9.43	4.44	3.15	1.31
Double-layered	1 (Low z)	9.44	3.10	2.15	1.17
	2 (High z)	9.41	4.02	2.90	1.51
Four-layered	1 (Low z)	9.44	4.56	3.41	1.88
	2	9.48	4.08	2.97	1.64
	3	9.47	4.14	3.00	1.66
	4 (High z)	9.44	4.43	3.23	1.70
Eight-layered	1 (Low z)	9.25	3.94	2.70	1.24
	2	9.18	3.74	2.69	1.49
	3	9.25	3.89	2.94	1.73
	4	9.28	3.84	2.91	1.59
	5	9.27	3.91	2.99	1.87
	6	9.25	3.86	2.92	1.74
	7	9.30	3.72	2.67	1.33
	8 (High z)	9.30	4.45	3.10	1.53

remains minimal across different Au layers within all three examined energy ranges. For example, when considering the energy range of [−2 eV, 0], we observe that the outermost Au layer (designated as "high z" in Table 1) exhibits only a slight increase of 0.29 labile electrons per atom compared to the Au layer at the interface with the C_3N_2 (marked as "low z"). This marginal difference in labile electrons persists across broader energy ranges as well, showing a difference of 0.400 e/Au for [−2.5 eV, 0] and 0.504 e/Au for [−3 eV, 0]. The 2- and 4-layer configurations follow this same trend. Focusing on the narrowest range beneath the Fermi level at the outermost layer, which contains those electrons most probably participating in catalysis, we find that the 4-layer configuration has the largest population of 1.70 e/Au, slightly larger than other configurations. This slight edge may translate to a marginally better catalytic performance.

Finally, we examine the bonding nature at the Au_x@C_3N_2 interface, focusing on the 8-layer configuration as a representative sample, using the charge density ρ (Fig. 5a) and the electron localisation function η (Fig. 5c). The ρ profile in the plane containing the Au–C bond at the interface, which is 3.01 Å long (Fig. 5c), indicates a diminishing charge density in the mid-bond region (marked with an arrow in Fig. 5b). Such a ρ profile rules out the formation of any covalent or metallic bond between Au and C. This is because, in metallic bonds, electrons are more or less uniformly distributed throughout the entire unit cell rather than being concentrated around any specific atomic centre. Similarly, covalent bonds, formed by the sharing of electron pairs between specific atoms, exhibit a higher electron density in the mid-bond region of the bonded atoms and lower electron density near the atomic centres.

The η profiles in Fig. 5c and d can provide further insight into the Au–C bonding characteristics. η is a numerical tool commonly used in solid-state physics and computational chemistry to analyse the electronic localisation trends in a material.[49] η provides information about the degree of localisation or delocalisation of electrons within a system, defined as a

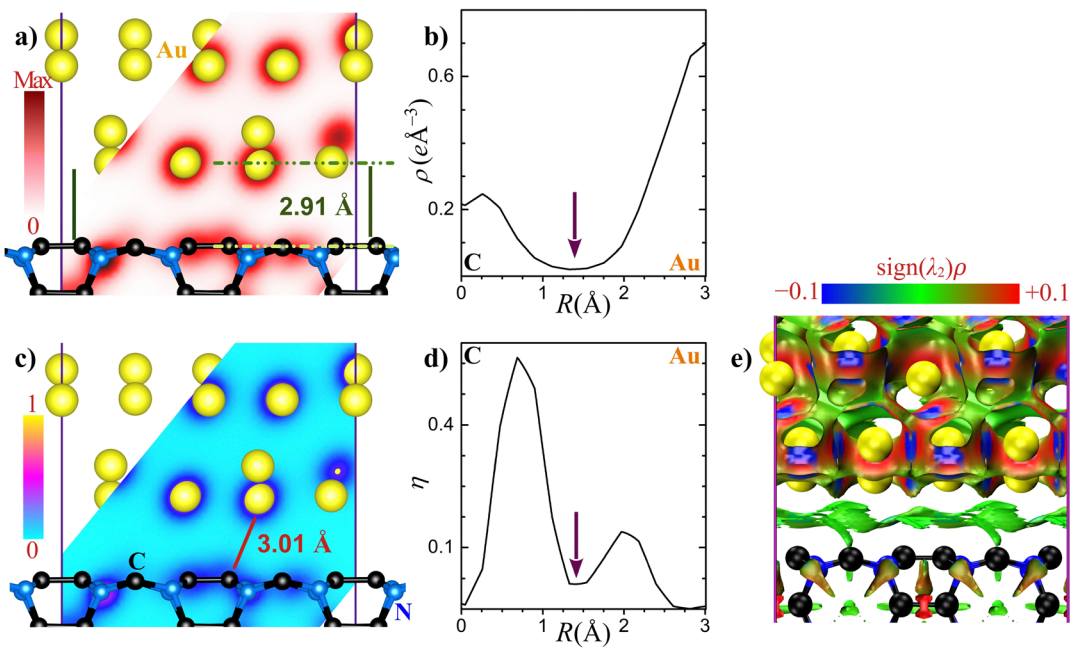

Fig. 5 (a) The charge density (ρ) visualised within a plane containing the interfacial Au–C bond. (b) The ρ profile along the Au–C bond. (c) The electron localisation function (η) visualised within the same plane as in (a). (d) The η profile along the Au–C bond. (e) The reduced density gradient iso-surface drawn at 0.5, and coloured based on the sign(λ_2)(ρ). The green iso-surface at the Au-C_3N_2 interface corresponds to an attractive van der Waals interaction.

function of the electron density as $\eta = [(1 + (D/D_h)^2)]^{-1}$ in which $D = \frac{1}{2}\sum_i |\nabla\varphi_i|^2 - \frac{1}{8}\left(\frac{|\nabla\rho|^2}{\rho}\right)$ and $D_h = \frac{3}{10}(3\pi^2)^{5/3}\rho^{5/3}$.[50] Here, φ_i are the Kohn–Sham orbitals and ρ the electronic density. Accordingly, since any region of strong electron localisation is accompanied by sharp changes in electron density, *i.e.*, high $|\nabla\rho|^2$, its η approaches 1. In contrast, regions with delocalised electrons tend to have more uniform ρ, smaller $\nabla\rho$ and consequently, in those regions, η approaches 0. As shown in Fig. 5d, η has two peaks, a primary peak near the C centre along the interfacial Au–C bond, and a smaller one near the Au centre, with a noticeable dip at the mid-bond region. Such behaviour again indicates a lack of covalent bonding. Note that covalent bonding is characterised by high electron localisation at the mid-bond region due to electron sharing, which is opposite to what is seen in Fig. 5d.

The analysis of ρ and η strongly suggests a lack of covalent or metallic bonding between Au and the CN support. Although ionic bonding can potentially be characterised by large ρ and η peaks at atomic centres, its successful formation depends on a significant charge transfer from cation to anion. In the case of $Au_x@C_3N_2$, the Bader charge analysis yields an electronic population of $\sim$10.98 *e* around Au atoms at the interfacial layer (low *z*); this charge is close to the total pseudopotential charge $5d^{10}6s^1$, and therefore, the possibility of any charge transfer from Au to C or N can be ruled out.

Given the circumstances, the only bonding mechanism that may act between Au and the C_3N_2 support should be based on dispersion effects. Indeed, when we repeated the cell relaxation without the dispersion effect included (IVDW = 0 in the VASP input file), the distance between Au and its C_3N_2 support increased to 3.81 Å. At this distance, no meaningful bonding is expected. Ultimately, we can confidently conclude that the bonding between Au and C_3N_2 is exclusively dispersion driven. Similar van der Waals bonding between Au nanosheets and carbon-based support (cellulose paper) has recently been reported.[51]

Furthermore, the nature of the Au and C_3N_2 interaction can be directly and visually assessed by plotting the non-covalent interaction.[52] This method exploits the fact that weak intermolecular contacts occur in real space where the electron density ρ is low. This low charge density, when accompanied by a near-zero reduced density, $S(r) = |\nabla\rho|/\{2(3\pi^2)^{1/3}\rho^{4/3}\}$, signals a region of density overlap that is neither a covalent bond nor a simple density tail. By plotting iso-surfaces of low *s* and colour-coding them with the sign of the second eigenvalue λ_2 of the Hessian of ρ, one obtains a visual map that directly distinguishes the nature of each interaction. This plot, calculated using the critic2 code[53–55] and presented in Fig. 5e, demonstrates the non-covalent, ergo the van der Waals, nature of the interaction at the interface.

4. Conclusion

We employed spin-polarised DFT-D3 calculations to investigate Au nanosheets supported on carbon nitride (C_3N_2), focusing on how the metal–support interface influences electronic structure and catalytic activity. Geometry optimisation shows the Au–C_3N_2 separation is $\sim$2.91 Å, indicating only weak van-der-Waals interaction with no covalent or metallic bonding, as confirmed by electron-localisation function (η), charge-density (ρ), and non-covalent interaction analyses. Bader charge analysis reveals an almost neutral Au charge ($\sim$10.98 *e*), ruling out significant charge transfer to the support. The Au 5d density of states remains unchanged mainly across different sheet thicknesses, demonstrating that the Au 5d population near the Fermi level is insensitive to the C_3N_2 substrate, even for the monolayer. Among the examined configurations, the four-layer $Au_x@C_3N_2$ slab offers the best compromise of weak Au-support hybridisation and the highest near-Fermi-level 5d occupation (1.7 *e* within the range of -2 eV and E_{Fermi}), which correlates with superior CO-oxidation activity. COHP analysis identified a clearly defined bonding hierarchy. O_2 binds strongly (ICOHP = 0.623 *e*/bond) on Au, whereas CO binds weakly (ICOHP = 0.037 *e*/bond). Nevertheless, co-adsorption markedly enhances the Au–CO interaction (ICOHP = 0.139 *e*/bond), confirming that O adsorption initiates CO activation and facilitates facile CO_2 release, which itself has negligible interaction with Au. Such a mechanism supports an efficient Langmuir–Hinshelwood pathway for CO oxidation. The results suggest that Au can be downsized to sub-nanometre dimensions without incurring the electron-deficiency penalties seen in other transition-metal systems, providing a viable strategy for designing stable, size-tuned Au catalysts on weakly interacting supports.

Conflicts of interest

There are no conflicts to declare.

Data availability

The data supporting the findings of this study, including input and output files from the DFT-D3 calculations, and density-of-states plots, can be made available upon request of the editor from the corresponding authors upon reasonable request. The earlier model of the C_3N_2 is available in the Materials Project database (*e.g.*, C_3N_2, mp-1188347). The Au@C_3N_2 models can be made available upon request of the editor from the corresponding authors.

Supplementary information (SI) is available. See DOI: https://doi.org/10.1039/d5ma01270h.

Acknowledgements

MHNA acknowledges TÜBİTAK's support for the 2221-visiting scientist fellowship. This research was further supported by funding from the Japan Science and Technology Agency (JST) and TÜBİTAK (Project No. 123N224) as the EIG CONCERT-JAPAN program under the project entitled 2023-MLALH. The HOKUSAI system at RIKEN, JAPAN, provided computational resources.

References

1 F. Gao and D. W. Goodman, *Chem. Soc. Rev.*, 2012, **41**, 8009.
2 E. Doustkhah, S. Rostamnia, N. Tsunoji, J. Henzie, T. Takei, Y. Yamauchi and Y. Ide, *Chem. Commun.*, 2018, **54**, 4402–4405.
3 Z. Chen, E. Vorobyeva, S. Mitchell, E. Fako, M. A. Ortuño, N. López, S. M. Collins, P. A. Midgley, S. Richard, G. Vilé and J. Pérez-Ramírez, *Nat. Nanotechnol.*, 2018, **13**, 702–707.
4 V. Malgras, H. Ataee-Esfahani, H. Wang, B. Jiang, C. Li, K. C. W. Wu, J. H. Kim and Y. Yamauchi, *Adv. Mater.*, 2016, **28**, 993–1010.
5 E. Doustkhah, H. Mohtasham, M. Farajzadeh, S. Rostamnia, Y. Wang, H. Arandiyan and M. H. N. Assadi, *Microporous Mesoporous Mater.*, 2020, **293**, 109832.
6 Y. Guo, M. Wang, Q. Zhu, D. Xiao and D. Ma, *Nat. Catal.*, 2022, **5**, 766–776.
7 S. K. Eswaramoorthy and A. Dass, *J. Phys. Chem. C*, 2022, **126**, 444–450.
8 P. Sharma, S. Kumar, O. Tomanec, M. Petr, J. Zhu Chen, J. T. Miller, R. S. Varma, M. B. Gawande and R. Zbořil, *Small*, 2021, **17**, 2006478.
9 C. Xiao, B.-A. Lu, P. Xue, N. Tian, Z.-Y. Zhou, X. Lin, W.-F. Lin and S.-G. Sun, *Joule*, 2020, **4**, 2562–2598.
10 E. Doustkhah, N. Tsunoji, M. H. N. Assadi and Y. Ide, *Adv. Mater. Interfaces*, 2023, **10**, 2202368.
11 W. Shi, A.-H. Park, H.-U. Park and Y.-U. Kwon, *J. Catal.*, 2020, **384**, 22–29.
12 J. Zhang, S. Yu, X. Liu, M. Wang, Z. Gao, X. Qin, Y. Xu, M. Wang and D. Ma, *J. Am. Chem. Soc.*, 2024, **146**, 34990–34997.
13 K. Sang, J. Zuo, X. Zhang, Q. Wang, W. Chen, G. Qian and X. Duan, *Green Energy Environ.*, 2023, **8**, 619–625.
14 E. Doustkhah, N. Tsunoji, S. Mine, T. Toyao, K. Shimizu, T. Morooka, T. Masuda, M. H. N. Assadi and Y. Ide, *ACS Appl. Mater. Interfaces*, 2024, **16**, 10251–10259.
15 X.-K. Wan, Z.-W. Lin and Q.-M. Wang, *J. Am. Chem. Soc.*, 2012, **134**, 14750–14752.
16 K. W. Qadir, M. Doust Mohammadi and H. Y. Abdullah, *Mater. Sci. Semicond. Process.*, 2025, **185**, 108973.
17 M. R. Narouz, K. M. Osten, P. J. Unsworth, R. W. Y. Man, K. Salorinne, S. Takano, R. Tomihara, S. Kaappa, S. Malola, C.-T. Dinh, J. D. Padmos, K. Ayoo, P. J. Garrett, M. Nambo, J. H. Horton, E. H. Sargent, H. Häkkinen, T. Tsukuda and C. M. Crudden, *Nat. Chem.*, 2019, **11**, 419–425.
18 D. Cheng, R. Liu and K. Hu, *Front. Chem.*, 2022, **10**, 958626.
19 G. A. Okon, D. G. Malu, H. Y. Abdullah, C. R. Nwokoye, N. I. Gber, C. P. Egbo, J. A. Unyime and T. E. Gber, *Diamond Relat. Mater.*, 2024, **149**, 111628.
20 G. Kresse and J. Furthmüller, *Comput. Mater. Sci.*, 1996, **6**, 15–50.
21 G. Kresse and J. Furthmüller, *Phys. Rev. B:Condens. Matter Mater. Phys.*, 1996, **54**, 11169–11186.
22 G. Kresse and D. Joubert, *Phys. Rev. B:Condens. Matter Mater. Phys.*, 1999, **59**, 1758–1775.
23 S. Grimme, J. Antony, S. Ehrlich and H. Krieg, *J. Chem. Phys.*, 2010, **132**, 154104.
24 S. Grimme, S. Ehrlich and L. Goerigk, *J. Comput. Chem.*, 2011, **32**, 1456–1465.
25 J. P. Perdew, K. Burke and M. Ernzerhof, *Phys. Rev. Lett.*, 1996, **77**, 3865–3868.
26 M. Fronzi, J. Bishop, A. A. Martin, M. H. N. Assadi, B. Regan, C. Stampfl, I. Aharonovich, M. J. Ford and M. Toth, *Carbon*, 2020, **164**, 51–58.
27 M. H. N. Assadi and H. Katayama-Yoshida, *Comput. Mater. Sci.*, 2017, **128**, 103–108.
28 S. Maintz, V. L. Deringer, A. L. Tchougréeff and R. Dronskowski, *J. Comput. Chem.*, 2016, **37**, 1030–1035.
29 R. Nelson, C. Ertural, J. George, V. L. Deringer, G. Hautier and R. Dronskowski, *J. Comput. Chem.*, 2020, **41**, 1931–1940.
30 S. R. Nath, S. S. Kurup and K. A. Joshi, *J. Comput. Chem.*, 2016, **37**, 1505–1510.
31 W. Tang, E. Sanville and G. Henkelman, *J. Phys.: Condens. Matter*, 2009, **21**, 084204.
32 A. Jain, S. P. Ong, G. Hautier, W. Chen, W. D. Richards, S. Dacek, S. Cholia, D. Gunter, D. Skinner, G. Ceder and K. A. Persson, *APL Mater.*, 2013, **1**, 011002.
33 S. Mohajer, M. A. Sharif, A. H. Aghdam, M. Borjkhani and M. H. N. Assadi, *Appl. Surf. Sci.*, 2023, **639**, 158120.
34 S. Jiao, X. Fu and H. Huang, *Adv. Funct. Mater.*, 2022, **32**, 2107651.
35 O. Johnson, *J. Catal.*, 1973, **28**, 503–505.
36 B. Hammer and J. K. Norskov, *Nature*, 1995, **376**, 238–240.
37 B. Hammer and J. K. Nørskov, in *Advances in Catalysis*, Elsevier, 2000, vol. 45, pp. 71–129.
38 M. Schalenbach, R. Tesch, P. M. Kowalski and R.-A. Eichel, *Phys. Chem. Chem. Phys.*, 2024, **26**, 14171–14185.
39 W. Xiao, K. Yoo, J. Kim and H. Xu, *ACS Nano*, 2024, **18**, 32732–32745.
40 F. Fang, Q. Cheng, M. Wang, Y. He, Y. Huan, S. Liu, T. Qian, C. Yan and J. Lu, *ACS Nano*, 2025, **19**, 1260–1270.
41 C. Martínez-Alonso and J. LLorca, *ACS Omega*, 2024, **9**, 29884–29895.
42 H. Xin, A. Vojvodic, J. Voss, J. K. Nørskov and F. Abild-Pedersen, *Phys. Rev. B:Condens. Matter Mater. Phys.*, 2014, **89**, 115114.
43 J. Wang, S. Xin, Y. Xiao, Z. Zhang, Z. Li, W. Zhang, C. Li, R. Bao, J. Peng, J. Yi and S. Chou, *Angew. Chem., Int. Ed.*, 2022, **61**, e202202518.
44 L. Mou, T. Han, P. E. S. Smith, E. Sharman and J. Jiang, *Adv. Sci.*, 2023, **10**, 2301020.
45 D.-H. Seo, J. Lee, A. Urban, R. Malik, S. Kang and G. Ceder, *Nat. Chem.*, 2016, **8**, 692–697.
46 M. H. N. Assadi, M. Fronzi, M. Ford and Y. Shigeta, *J. Mater. Chem. A*, 2018, **6**, 24120–24127.
47 N. Luo, Z. Hou, C. Zheng, Y. Zhang, A. Stein, S. Huang and D. G. Truhlar, *Chem. Mater.*, 2021, **33**, 834–844.
48 K. Suraj and M. Assadi, Volume 44: Energy Transitions toward Carbon Neutrality: Part VII, 2024, preprint, 10.46855/energy-proceedings-11059.
49 J. W. Furness, U. Ekström, T. Helgaker and A. M. Teale, *Mol. Phys.*, 2016, **114**, 1415–1422.

50 B. Silvi and A. Savin, *Nature*, 1994, **371**, 683–686.
51 E. J. Jeong, E. Im, D. C. Hyun, J. W. Lee and G. D. Moon, *J. Ind. Eng. Chem.*, 2020, **89**, 204–211.
52 J. Contreras-García, R. A. Boto, F. Izquierdo-Ruiz, I. Reva, T. Woller and M. Alonso, *Theor. Chem. Acc.*, 2016, **135**, 242.
53 E. R. Johnson, S. Keinan, P. Mori-Sánchez, J. Contreras-García, A. J. Cohen and W. Yang, *J. Am. Chem. Soc.*, 2010, **132**, 6498–6506.
54 A. Otero-de-la-Roza, E. R. Johnson and J. Contreras-García, *Phys. Chem. Chem. Phys.*, 2012, **14**, 12165.
55 A. Otero-de-la-Roza, E. R. Johnson and V. Luaña, *Comput. Phys. Commun.*, 2014, **185**, 1007–1018.